

Article

One Pot Synthesis, Surface and Magnetic Properties of Cu₂O/Cu and Cu₂O/CuO Nanocomposites

Sameerah I. Al-Saeedi ¹, Ghadah M. Al-Senani ¹ , Omar H. Abd-Elkader ^{2,3,*}  and Nasrallah M. Deraz ⁴

¹ Department of Chemistry, College of Science, Princess Nourah Bint Abdulrahman University, P.O. Box 84428, Riyadh 11671, Saudi Arabia; sialsaeedi@pnu.edu.sa (S.I.A.-S.); gmalsnany@pnu.edu.sa (G.M.A.-S.)

² Physics and Astronomy Department, Science College, King Saud University, P.O. Box 2455, Riyadh 11451, Saudi Arabia

³ Physics Division, Electron Microscope and Thin Films Department, National Research Centre, El Behooth St., Giza 12622, Egypt

⁴ Physical Chemistry Department, National Research Centre, El Behooth St., Giza 12622, Egypt; amn341@yahoo.com

* Correspondence: omabdelkader7@ksu.edu.sa

Abstract: A series of copper-based systems containing two different nanocomposites (Cu₂O/CuO and Cu₂O/Cu) was synthesized by the egg white assisted auto-combustion route. This method was distinguished by the simplicity of its steps, low cost, one-pot synthesis process at low temperature and, short time. The characterization of the as prepared nanocomposites was carried out by using X-ray diffraction (XRD), Fourier-transform infrared (FTIR), Scanning electron microscope (SEM) and transmission electron micrograph (TEM), Energy dispersive spectrometry (EDS) techniques. Surface and magnetic properties of the obtained systems were determined by using N₂ adsorption/desorption isotherms at 77 K and the vibrating sample magnetometer (VSM) technique. XRD results confirmed the formation of Cu₂O/CuO and Cu₂O/Cu nanocomposites with different ratios of well crystalline CuO, Cu₂O, and Cu phases. FTIR results of the combusted product displays the presence of both CuO and Cu₂O, respectively. SEM/EDS and TEM results confirm the formation of a porous nanocomposite containing Cu, O, and C elements. The change in concentration of the oxygen vacancies at the surface or interface of both Cu₂O/CuO and Cu₂O/Cu nanoparticles resulted in different changes in their magnetization. Based on this study, it is possible to obtain nanocomposite-based copper with multiple valances by a simple and inexpensive route which can be suitable for the fabrication of different transition metal composites.



Citation: Al-Saeedi, S.I.; Al-Senani, G.M.; Abd-Elkader, O.H.; Deraz, N.M. One Pot Synthesis, Surface and Magnetic Properties of Cu₂O/Cu and Cu₂O/CuO Nanocomposites. *Crystals* **2021**, *11*, 751. <https://doi.org/10.3390/cryst11070751>

Academic Editors: Assem Barakat and Alexander S. Novikov

Received: 7 June 2021

Accepted: 21 June 2021

Published: 26 June 2021

Publisher's Note: MDPI stays neutral with regard to jurisdictional claims in published maps and institutional affiliations.



Copyright: © 2021 by the authors. Licensee MDPI, Basel, Switzerland. This article is an open access article distributed under the terms and conditions of the Creative Commons Attribution (CC BY) license (<https://creativecommons.org/licenses/by/4.0/>).

Keywords: Cu₂O/Cu; Cu₂O/CuO; nanoparticles; XRD; FTIR; SEM; TEM; EDS; VSM

1. Introduction

Copper oxide nanoparticles (CuO and Cu₂O NPs) have a wide range of uses in the environmental and industrial domains. This could be owing to the unique physical and chemical properties of specific particles, such as spin dynamics and high-temperature superconductivity [1]. CuO and Cu₂O represent, in actuality, p-type transition metal semiconducting materials with band gaps of 1.7 and 2.7 eV, respectively [2,3]. They appear to be having unique mechanical, electrical, and magnetic characteristics. These particles are then utilized as heterogeneous catalysts, antioxidants, drug delivery agents, including imaging agents, throughout the biopharmaceutical industry [4–6]. Furthermore, Cu-based nanoparticles have been developed to improve the viscosity of energy-transfer fluids, consequently increasing thermal conductivity [7]. Thermoelectric materials, sensing materials, glass, ceramics, ceramic resistors, magnetic storage media, gas sensors, near-infrared filters, photoconductive and photothermic applications, semiconductors, solar energy transformation, and high-tech superconductors could all benefit with them [8,9]. All of these applications can be enhanced by accurately optimizing the particle size and dissipation

in the nanoscale. On the other hand, information on the synthesis and description of $\text{Cu}_2\text{O}/\text{CuO}$ nanoparticles are very important for understanding the unique properties of these particles depending on the coexistence of two oxides together. At the interfaces of these oxides, some phenomena such as exchange interactions appeared, affecting most of the physical and chemical properties of the prepared composite.

$\text{Cu}_2\text{O}/\text{CuO}$ NPs of various shapes and sizes have been synthesized using a variety of physical and chemical processes, including electrochemical, sonochemical, sol-gel, micro emulsion, precipitation, and microwave irradiation [10–17]. Consequently, employing traditional techniques to make $\text{Cu}_2\text{O}/\text{CuO}$ and $\text{Cu}_2\text{O}/\text{Cu}$ nanoparticles resulted in instability of both Cu and Cu_2O nanoparticles. The instability of these particles is due to its easy oxidation in aqueous medium [9]. To avoid the surface oxidation of copper nanoparticles, material researchers have long focused on green methodologies for nanomaterial manufacturing [18]. As a consequence, finding an appropriate and environmentally friendly natural product, and perhaps an environmentally responsible, suitable solvent, is one of the most challenging tasks in the green synthesis of metal nanoparticles. Among these products, the plants containing bioactive compounds can be used as a reducing, stabilizing, and capping agents during the preparation process [10]. Similar results reported that the preparation of copper-based composites via the thermal decomposition method with an organic surfactant (fatty acids), e.g., oleic acid and oleylamine, resulted in the protection of copper nanoparticles against the oxidation process. The oleic acid-assisted thermal decomposition approach resulted in the stabilization and manufacture of $\text{Cu}/\text{Cu}_2\text{O}$ nanoparticles, according to the observations. Cu nanoparticles are synthesized just after the thermal decomposition of copper acetate monohydrate in the presence of both oleic acid and oleylamine [11]. This work established a new green synthesis process based on egg white for both $\text{Cu}_2\text{O}/\text{CuO}$ and $\text{Cu}_2\text{O}/\text{Cu}$ Cu_2O and CuO nanoparticles. This process allowed to overcome the previous complications.

Furthermore, the low-temperature magnetic characteristics of $\text{Cu}_2\text{O}/\text{CuO}$ NPs strongly indicated that these particles have ferromagnetic (FM) behavior patterns, suggesting that they're used in significant spintronic applications [19]. Recognizing the concept of ferromagnetic room temperature (RTFM) in semiconducting or insulating materials, unfortunately, is one of most pressing issues. Anion/cation vacancies and/or quantum confinement mechanisms can indeed be the source of FM in these systems. Moreover, the dispute over the origins of FM character persists [20,21]. There is little doubt that the technology used to prepare nanoparticles will have a significant effect on the RTFM of these particles, enabling them to be used for spintronic devices as well as other applications.

The goal of this study was to use an egg white assisted auto-combustion technique to produce $\text{Cu}_2\text{O}/\text{CuO}$ and $\text{Cu}_2\text{O}/\text{Cu}$ NPs. The morphological, surface, and magnetic properties of the produced NPs were also evaluated.

2. Materials and Methods

2.1. Materials

Sigma-Aldrich Company (Darmstadt, Taufkirchen, Germany) provided the chemical material, copper (II) nitrate trihydrate with the linear formula $\text{Cu}(\text{NO}_3)_2 \cdot 3\text{H}_2\text{O}$. This reagent had not been refined further. Fresh egg white from regional chickens was used to develop egg white.

2.2. Preparation Route

Through incorporating a calculated amount of copper nitrate (2.426 g) with concentrated solutions of egg white, four samples of copper oxides were synthesized (0, 5, 10, and 15 mL). The homogeneous precursors were subsequently concentrated on a hot plate for 5 min in a porcelain crucible at 300 °C for 10 min. The crystal water was smoothly vaporized, and much foam was generated by convection. Whenever the crucible temperature reached 300 °C, a spark ignited at one side and propagated throughout the mass, producing a voluminous and chunky substance within the crucible. In this study, the

ratios of the egg white: copper nitrates were (0, 5, 10, 15 mL): 2.426g for S1, S2, S3, and S4 samples, respectively.

2.3. Characterization Techniques

The X-ray analysis of distinct mixed solids was performed by using a BRUKER D8 advance diffractometer (Bruker, Karlsruhe, Germany). The patterns were run at 40 kV and 40 mA with 2 theta 2° min^{-1} scanning speeds with Cu $K\alpha$ radiation. Equations (1)–(4) have been used to obtain the mean crystallite size (d), dislocation density (δ), stress (ϵ), and strain (σ) of CuO, Cu₂O, and Cu present in the analyzed composites based on X-ray diffraction line broadening as follows [22,23]:

$$d = 0.89 \lambda / \beta \cos\theta \quad (1)$$

$$\delta = 1/d^2 \quad (2)$$

$$\epsilon = \beta \cos\theta / 4 \quad (3)$$

$$\sigma = \epsilon Y \quad (4)$$

where d is the average crystallite size of the phase under study, 0.89 is the Scherrer constant, β is the complete breadth at half the height of the peaks in radians, θ is the diffraction angle in radians, Y is Young's modulus, and λ is the X-ray wavelength in nanometer scale.

Using the PerkinElmer Spectrophotometer, the investigated solid's Fourier-transform infrared (FTIR) spectrum was obtained (PerkinElmer, Coraopolis, PA, United States). At wavelengths ranging from 4000 to 400 cm^{-1} , the IR spectra were recorded. A total of 200 mg of vacuum-dried potassium bromide (KBr) IR was combined with 2 mg of solid samples. The mixture was placed as a 13 mm diameter disk into some kind of steel die and forced to 12-ton pressure after already being dispersed for 3 min in a vibrating ball mill. The sample disk was inserted into the holder of a double grating IR spectrometer.

Scanning electron microscope (SEM) and transmission electron micrograph (TEM) images were captured using JEOL JAX-840A and JEOL Model 1230 (JEOL, Tokyo, Japan), respectively, and a particle disperser unit was used to disperse individual particles over the mounted SEM setup. This will allow an even distribution of the sample on the sticker, reducing the incidence of overlapping particles and generating a pattern that can be used to study granulometry. For TEM using a micropipette, a single drop of the sample was placed on 300 mesh grids covered with holey carbon (Carbon coated copper grids). The samples were dispersed in ethanol and then treated ultrasonically for a few minutes.

With a Delta Kevex device attached to an electron microscope, JED- 2200 Series, energy dispersive X-ray analysis (EDS with Mapping) was performed (JEOL, Tokyo, Japan). The following parameters were used: accelerating voltage of 25 kV, accumulation time of 120 s, and window width of 6 μm . The surface molar composition was calculated using the Asa approach, Zaf-correction, and Gaussian approximation.

The surface properties, namely specific surface area (S_{BET}), total pore volume (V_{P}), and mean pore radius (\hat{r}) of different samples were determined from nitrogen adsorption isotherms at 77 K using a conventional volumetric apparatus Brunnauer–Emmett–Teller method (Microtrac Retch GmbH Retsch-Allee 1-5 42781 Haan Germany). Before carrying out the measurements, each sample was out-gassed under a reduced pressure of 10^{-5} Torr at 200 $^\circ\text{C}$ for 2 h.

The magnetic characteristics of the materials evaluated in a maximum field of 20 kOe were investigated by using a vibrating sample magnetometer (VSM) (9600-1 LDJ, Weistron Co., Ltd., West Hollywood, CA, USA). Hysteresis loops, saturation magnetization (M_{s}), remanence magnetization (M_{r}), and coercivity (H_{c}) were identified.

3. Results

3.1. XRD Study

X-ray measurements are used to shed light on the crystal structure and phase analysis of the as-prepared solids. Figure 1 depicts XRD patterns of the S1, S2, S3, and S4 samples. This figure shows that the as-synthesized solids contain well crystalline monoclinic CuO (PDF no: 801917), cubic Cu₂O (PDF no: 782026 and 851326), and cubic Cu (PDF no: 050667) phases with different ratios. The Miller indices (hkl) and two theta (2 Θ) of these crystallites in various composites were matched with that of the same crystallites in the PDF Files deposited in a database. The powder diffraction file (PDF) is a single-phase X-ray powder diffraction patterns characteristic interplanar spacing and corresponding relative intensities along other physical and crystallographic properties.

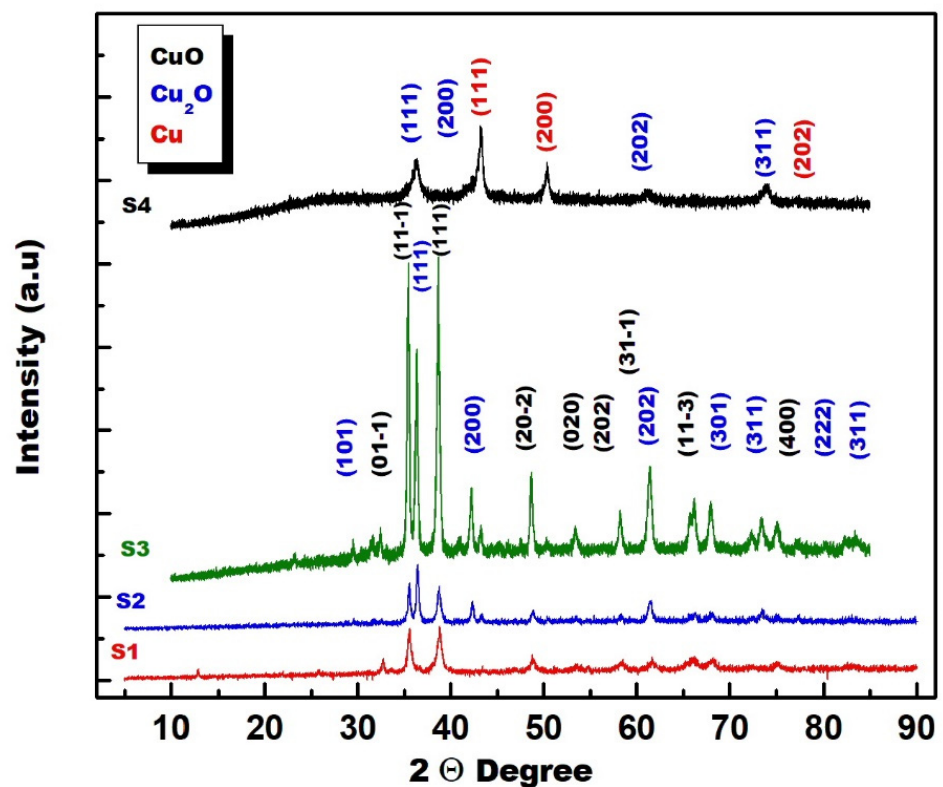


Figure 1. X-ray Diffraction Patterns (XRD) patterns of the S1, S2, S3 and S4 samples.

Inspection of Figure 1 reveals that: (i) The S1, S2, and S3 samples consisted of CuO and Cu₂O phases with different abundance. This indicates that these samples are composites composed of Cu₂O/CuO. The dominant CuO peaks were observed in the S1, S2, and S3 samples. (ii) The addition of 5 mL egg white and/or increasing of its amount from 5 mL to 10 mL during the preparation process resulted in an enhancement in the peak height of Cu₂O, as shown in the S2 and S3 samples. This suggests that cupric oxide is gradually transformed into cuprous oxide. (iii) The S4 sample displays the formation of Cu₂O/Cu composite with subsequent disappearance of CuO phase. (iv) Changes in the amount of egg white used resulted in a shift in the positions of diffraction peaks, as well as changes in their intensities, indicating that the manufactured composites' characteristics had modified. (v) Egg white assisted combustion at 300 °C for 15 min often resulted in contamination of the as-prepared samples by carbon traces. However, the XRD technique cannot determine this carbon due to its small amount.

Changing the amount of egg white used in the assisted auto-combustion approach resulted in the formation of Cu₂O/Cu and Cu₂O/CuO nanocomposites, according to these results. Previous research, on either side, found that employing a particular amount

of glycine accelerated auto-combustion, resulting in the production of a nanocrystalline CuO/Cu₂O/Cu system. [24]. The Fullprof crystallographic programs are used to detect the lattice parameters (unit cell dimensions, crystal system, and space group) and other crystallographic parameters [25]. XRD data enabled us to calculate the strain (E), stress (σ), dislocation density (δ), X-ray density (D_x), and crystallite size (d) of the constituents (CuO, Cu₂O, and Cu) of various copper-based composites. These parameters are presented in in Tables 1 and 2. It can be seen from these tables that: (i) Increased egg white concentration caused an increase in several lattice constants (c and b) of CuO particles, and even an increase in their volume, diameter, and density, indicating grain evolution. By increasing the amount of egg white supplied, this grain development led to quite an increase in the peak height of CuO. (ii) There are no clear changes in the lattice parameters of Cu₂O by increasing the egg white content. So, the increase in peaks height of Cu₂O could be attributed to the increase in its amount, indicating the transformation of some CuO to Cu₂O. (iii) Increasing egg white up to 10 mL resulted in an increase in the values of dislocation, strain, and stress for CuO particles. The opposite behavior was observed in case of Cu₂O particles. However, this treatment led to an increase in the crystallite size of both CuO and Cu₂O. (iv) Synthesis of Cu₂O/Cu composite by using 15 mL egg white brought about an increase in the values of E , σ and δ for both CuO and Cu₂O particles. In addition, the crystallite size of Cu₂O particles in the Cu₂O/Cu composite is smaller than that of this oxide in Cu₂O/CuO composites.

Table 1. Crystal parameters, detected phases and their PDF files for S1, S2, S3 and S4 samples.

Crystal Parameters	a (Å)	b (Å)	c (Å)	α (°)	β (°)	γ (°)	Volume (Å ³)	Density (g/cm ³)	Space Group	Phases
S1	5.1274	3.4231	4.6775	90.05	99.50	89.89	80.9717	6.499	Monoclinic Cc [9]	CuO (PDF 801917)
	4.2667	4.2667	4.2667	90	90	90	77.67	6.117	Cubic Pn3m [224]	Cu ₂ O (PDF 782026)
S2	4.6897	3.4289	5.1350	90	99.5	90	81.4409	6.507	Monoclinic C2/c [15]	CuO (PDF 801917)
	4.2594	4.2594	4.2594	90	90	90	77.276	6.156	Cubic Pn3m [224]	Cu ₂ O (PDF 782026)
S3	4.6897	3.4287	5.1343	90	99.5	90	81.3782	6.507	Monoclinic C2/c [15]	CuO (PDF 801917)
	4.2605	4.2605	4.2605	90	90	90	77.330	6.156	Cubic Pn3m [224]	Cu ₂ O (PDF 782026)
S4	8.9096	8.9096	8.9096	90	90	90	70.725	8.935	Cubic Fm3m [225]	Cu (PDF 050667)
	4.2556	4.2556	4.2556	90	90	90	77.060	6.156	Cubic Pn3m [224]	CuO (PDF 801917)

Table 2. Crystallite size, dislocation, stress and strain of Cu, Cu₂O and CuO crystallites.

Sample	Crystallite Size (nm)	δ (Lines/nm ²)	ϵ	σ (N/m ²)	Phases
S1	38.494868	6.75×10^{-4}	9.00×10^{-4}	0.117	CuO (PDF 801917)
	38.505532	6.74×10^{-4}	9.00×10^{-4}	0.176	Cu ₂ O (PDF 782026)
S2	25.876072	1.49×10^{-3}	1.34×10^{-3}	0.1742	CuO (PDF 801917)
	41.395075	5.84×10^{-4}	8.37×10^{-4}	0.1029	Cu ₂ O (PDF 782026)
S3	51.134580	3.82×10^{-4}	6.78×10^{-4}	0.08814	CuO (PDF 801917)
	50.978162	3.85×10^{-4}	6.80×10^{-4}	0.08364	Cu ₂ O (PDF 782026)
S4	32.006909	9.76×10^{-4}	1.08×10^{-3}	0.13284	Cu ₂ O (PDF 782026)
	23.610946	1.79×10^{-3}	1.47×10^{-3}	0.19551	Cu (PDF 050667)

3.2. FTIR Analysis

The FTIR spectra of different copper systems synthesized by egg white-assisted auto-combustion are presented in Figure 2. In addition, this figure displays the FTIR of KBr

material which blended with 2 mg of solid samples. This measurement was taken to demonstrate the functional groups on the surface of the analyzed specimens in the $4000\text{--}400\text{ cm}^{-1}$ range. The positions of the observed bands and their intensities in these spectra were altered based on the synthesis process and the egg white content. Some sharpness bands located at $469\text{--}462$, $605\text{--}600$, $876\text{--}825$, and 1054 cm^{-1} were ascribed the Cu(II)–O bond vibrational frequencies in CuO [26]. Other bands were observed at $629\text{--}618$, $710\text{--}702$, and $780\text{--}760\text{ cm}^{-1}$ due to Cu(I)–O stretching of Cu_2O particles [27]. Additional bands confirm the presence of carbon traces observed at 2198 and 2924 cm^{-1} due to C–H stretching vibrations [28]. Stretching and bending vibrations of hydroxyl groups (O–H) due to the adsorption of water molecules from the air on the surface of the produced solids containing both carbon traces and KBr might be attributed to the bands observed at $1128\text{--}1054$, $1629\text{--}1580$, and $3493\text{--}3433\text{ cm}^{-1}$ [29,30]. The FTIR spectrum for KBr only displays the previous bands that belong to OH groups due to the adsorption of water molecules on KBr surface. However, the group of OH are adsorbed by carbon traces.

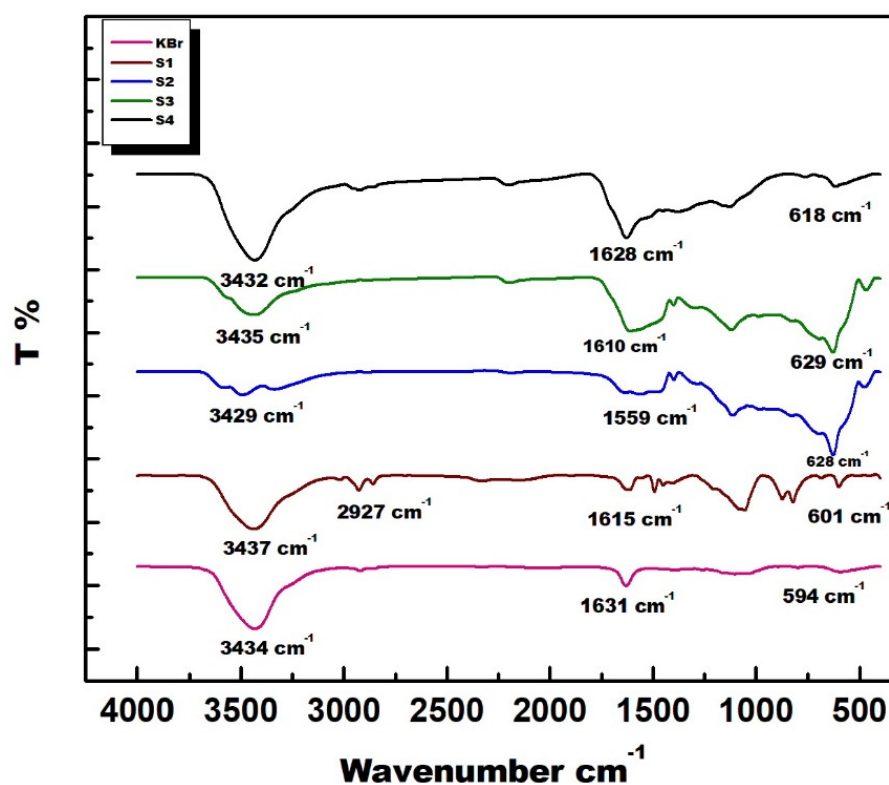


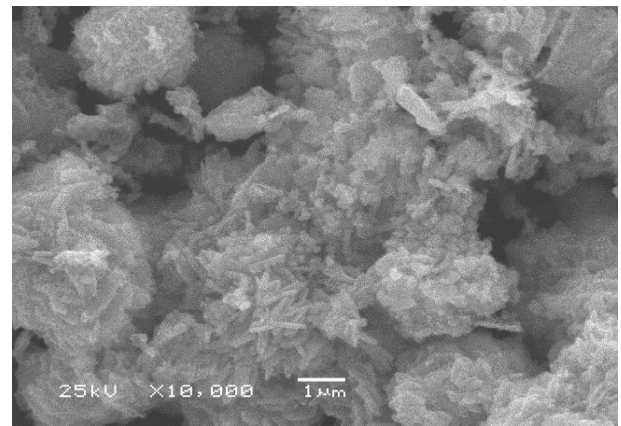
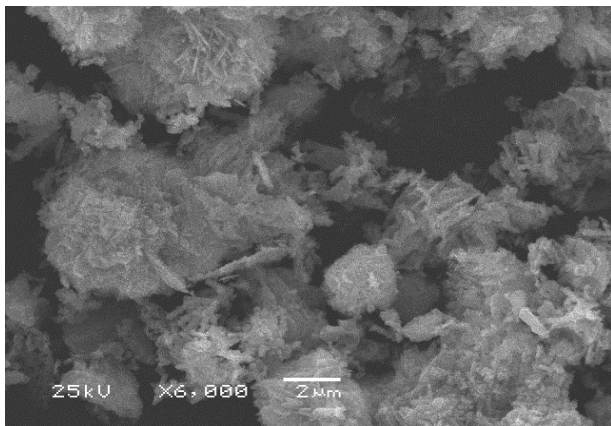
Figure 2. Fourier-transform infrared (FTIR) spectrum of the S1, S2, S3 and S4 samples.

3.3. SEM/EDS and TEM Analyses

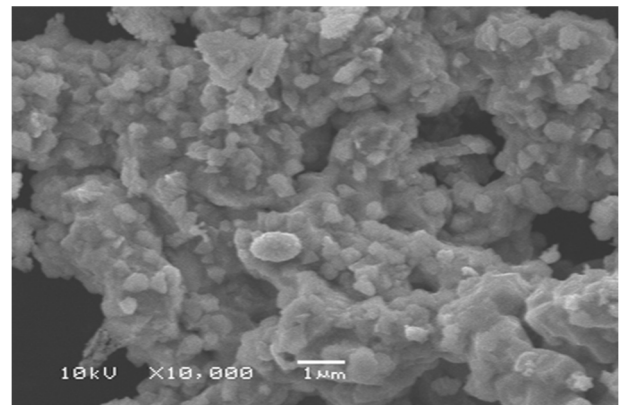
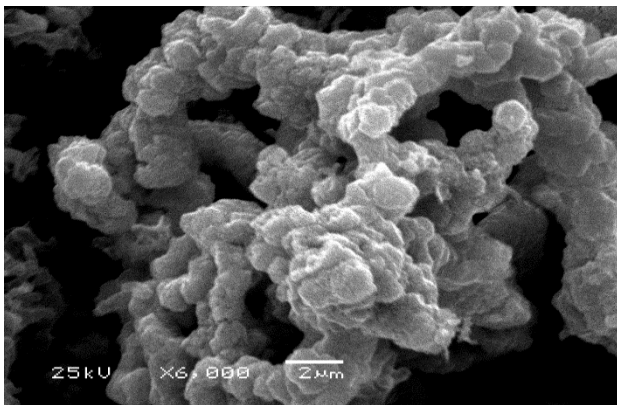
SEM can be used to identify the morphology of the materials under investigation. Figure 3 shows the surface morphology of the S1, S2, S3, and S4 specimens at various magnifications. This figure indicates that the as-prepared samples were composed of different particles. The S1 sample consisted of aggregated slats or panels and semi-spherical particles. The S2 sample also contains semi-spherical particles deposited on the surface of condensed particles of highly agglomerated particles or fused particles. In the SEM image of the S3 sample, the formation of aggregated polyhedron particles with some spherical particles over the agglomerated particles can be seen. Finally, some spherical particles over the condensed sheet containing some voids were observed in the case of S4 samples. Thus, one can speculate that the spherical particles are Cu_2O , while the fused particles are Cu depending on the brightness of these particles. However, all SEM images confirm that the

studied samples are porous materials. In addition, SEM images indicate that the prepared solids can appear as composites based on the presence of the two types of particle.

The elemental analysis of the S1, S2, S3, and S4 specimens was investigated, and the results are presented in Figure 4. This analysis confirms that the S2, S3, and S4 specimens contained different concentrations of Cu, O, and C elements (inset tables in Figure 4) based on the amount of egg white utilized in the synthesis procedure. The S1 sample, on either hand, mainly contains Cu and O components. The elemental mapping method was used to establish the distribution of these elements, which is based on accumulating extremely precise elemental composition data over the surface areas of samples.



S1



S2

Figure 3. Cont.

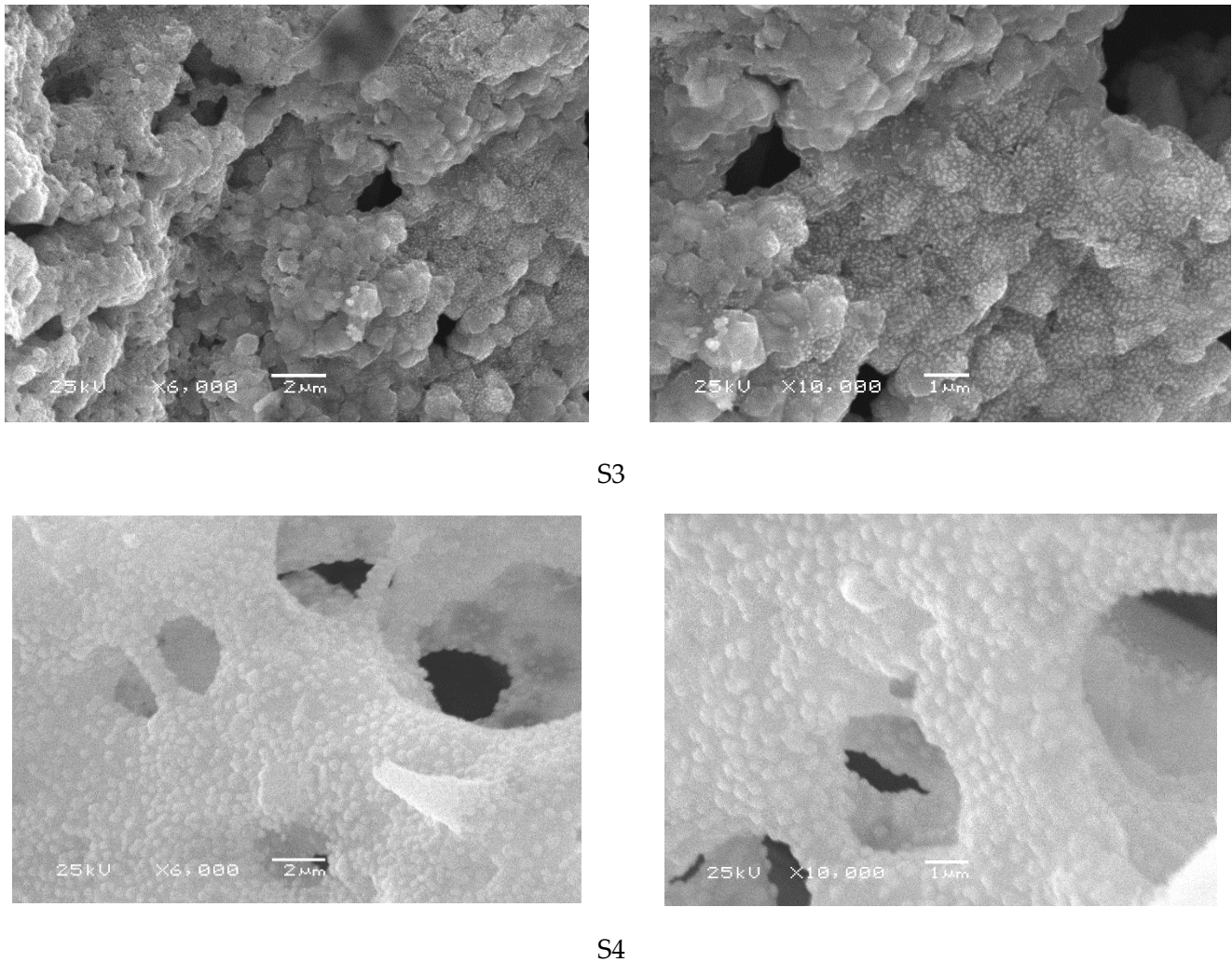
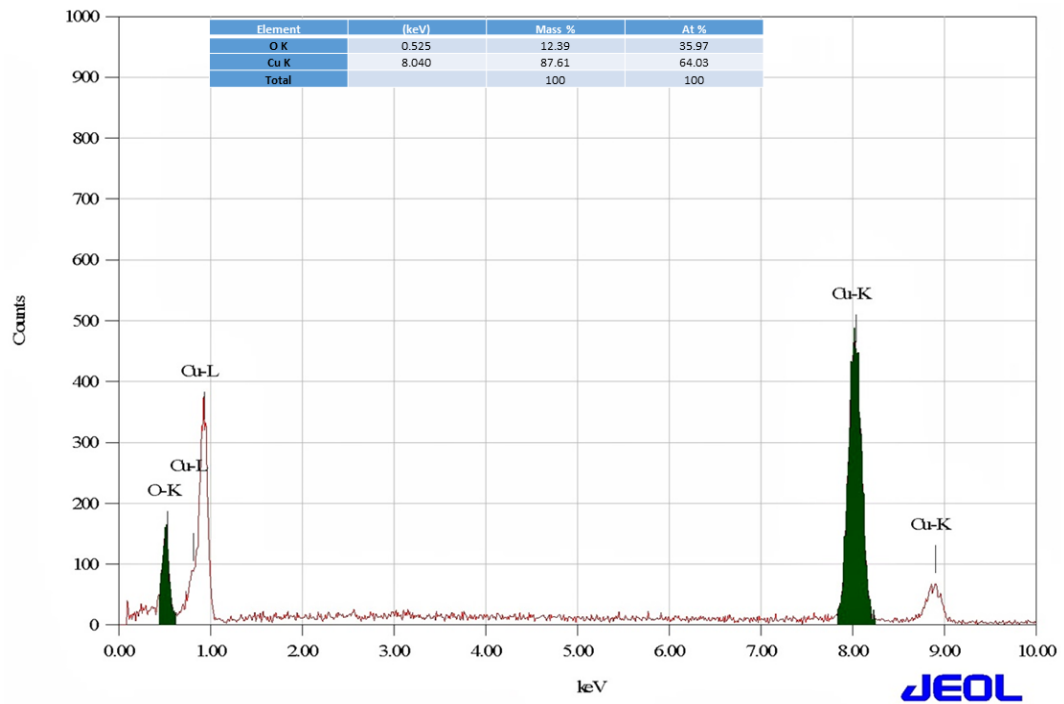


Figure 3. Scanning electron microscopy (SEM) images with different magnifications of the S1, S2, S3 and S4 samples.

Elemental mapping is based on accumulating extremely specific elemental composition data across a sample area to provide high-resolution imaging via elemental composition data. Every pixel in the digital image is scanned to maintain the existing elemental spectrum, transform the relative intensity into computed colorization layers, with color code, and show layers and sites of elemental compositional information. EDS mapping analyses of the various samples investigated are presented in Figure 5. The analysis of the elemental composition was executed with respect to several different locations, as shown in SEM images (Figure 5 (S1a, S2a, S3a, S4a)). Figure 5 (S1b, c) display homogeneity in the distribution of Cu and O elements, which build the whole body of the prepared samples. Figure 5 S2–S4: (b–d) show the distribution homogeneity of Cu, O, and C elements for samples S2, S3, and S4, respectively. The corresponding results are presented separately for each element. The amount of dispersed carbon increases with the egg white content, despite the fact that this was not apparent in the figures. The change throughout the distribution of both oxygen and copper elements at the uppermost surface layers was associated with an increase in the distributed carbon content accompanied by an increase in the reduction process for copper nanoparticles. From the elemental mapping investigation, it is clearly seen that elements are properly distributed in the aggregated $\text{Cu}_2\text{O}/\text{Cu}$ and $\text{Cu}_2\text{O}/\text{CuO}$ nanocomposites.

S1



S2

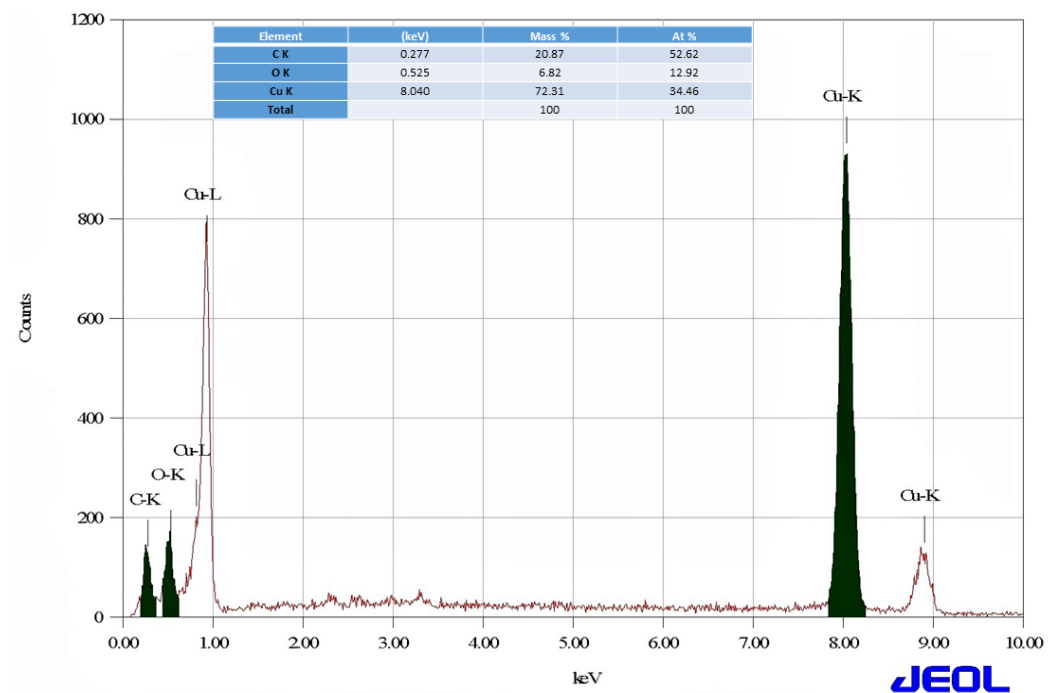
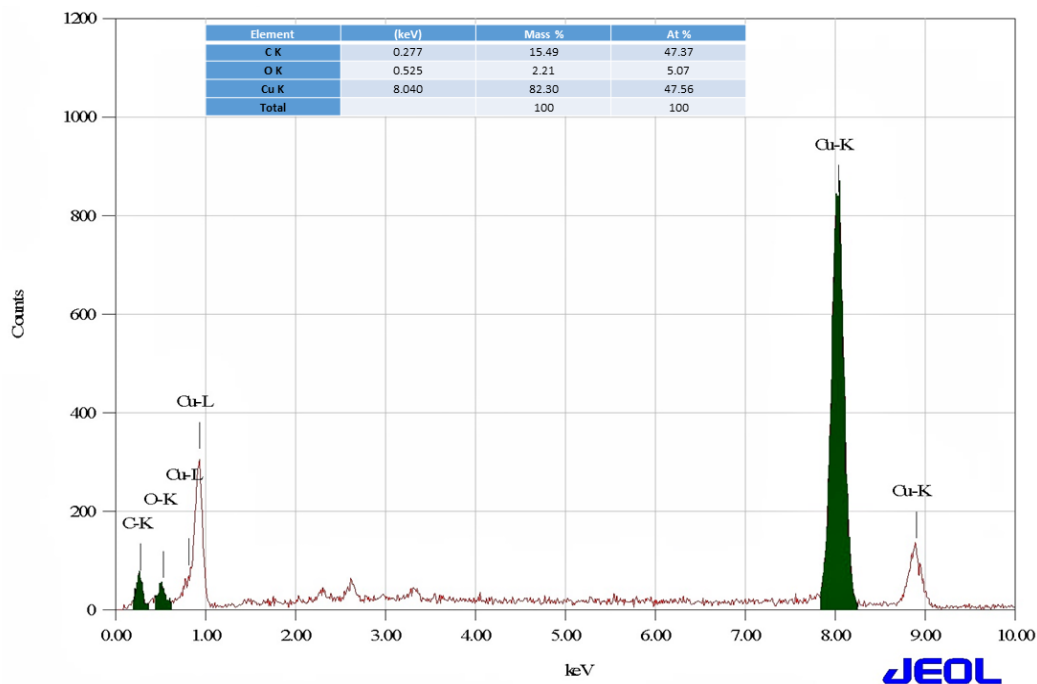


Figure 4. Cont.

S3



S4

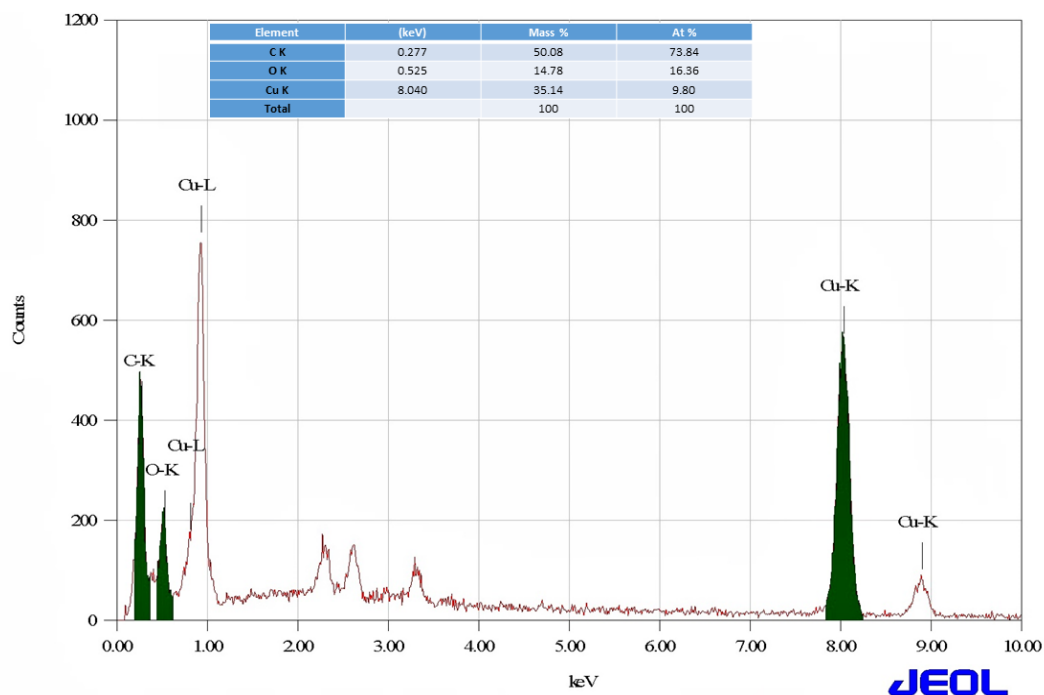


Figure 4. Energy dispersive spectrometry (EDS) patterns of the S1, S2, S3 and S4 samples.

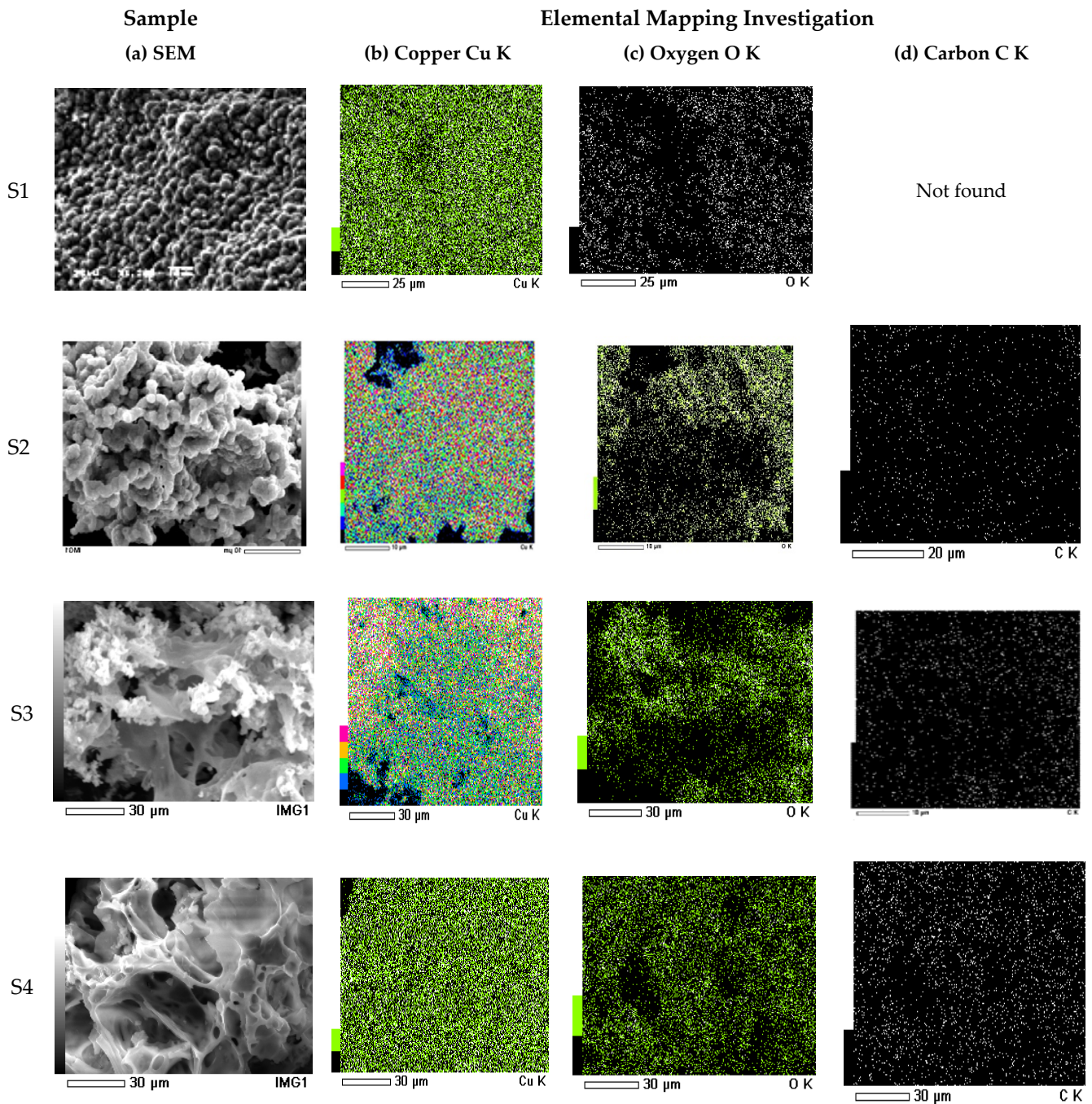
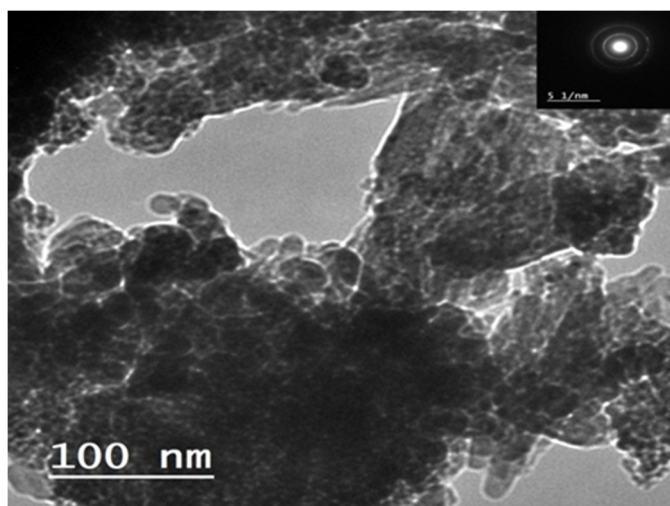


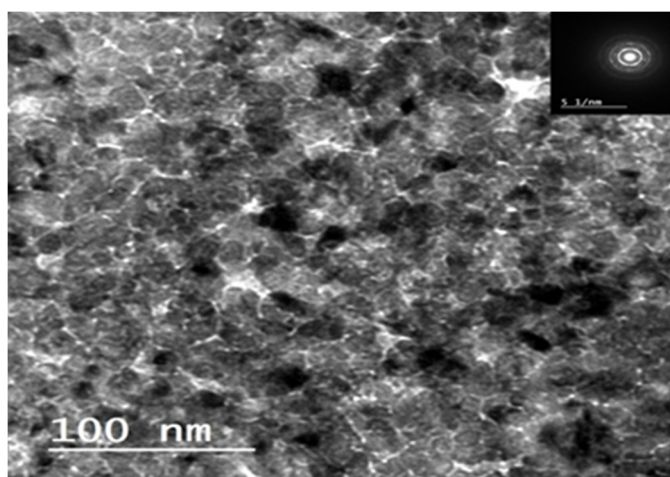
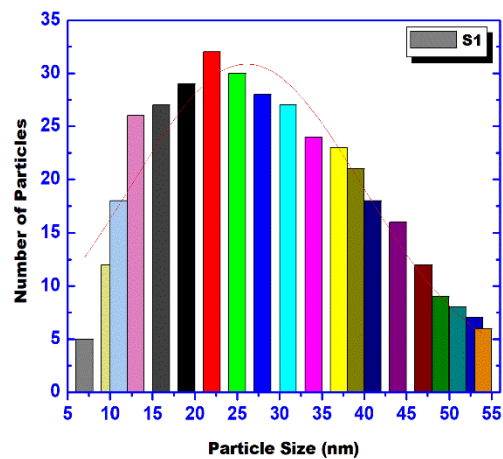
Figure 5. Energy dispersive spectrometry (EDS) elemental mapping analyses of the samples S1, S2, S3 and S4: (a) SEM, (b) Copper distribution, (c) Oxygen distribution, and (d) Carbon distribution.

TEM analysis was carried out on the S1, S2, S3, and S4 samples to shed more light on the shape and nature of their particles as shown in Figure 6a,b. The TEM image of the S2 sample shows many groups of spherical like nanoparticles between the different voids. It can be seen that most particles in the S1, S2, and S4 samples have spherical shape. However, the TEM image of the S3 sample displays small spheres and polyhedron shape similar to cubic structures. The porosity in the S2 sample is greater than that in the other samples. The TEM image of the S1, S2, S3, and S4 samples enabled us to illustrate their particle size distribution in Figure 6. It can be seen from this figure that the particles are in the nano scale with average grain size in the range of 17–50 nm, confirming XRD results. The particle nature can be determined by a crystallographic experimental technique involving

transmission electron microscopy. This technique enabled us to study the selected area electron diffraction (SAED, the inset of Figure 6) for the S1, S2, S3 and S4 samples. SAED patterns display a set of rings containing different spots. This observation confirms the polycrystalline structure observed by the XRD technique.



(a)



(b)

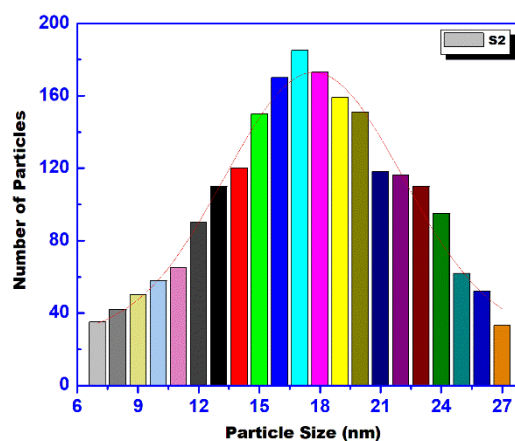


Figure 6. Cont.

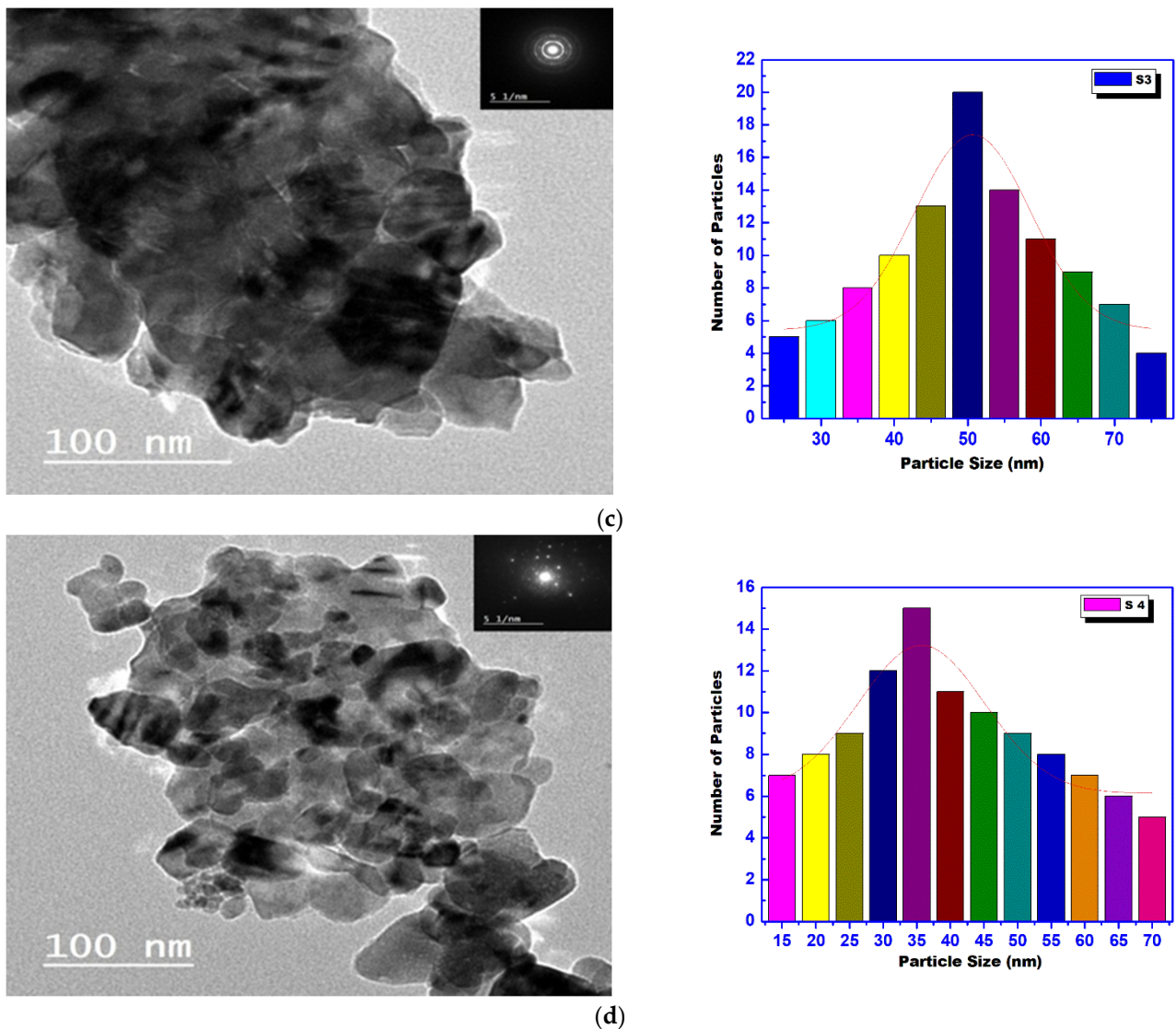


Figure 6. Transmission electron micrograph (TEM) images and particle size distribution of the (a) S1, (b) S2, (c) S3 and (d) S4 samples.

3.4. Surface Characteristics

Surface properties of the S1, S2, S3, and S4 samples were evaluated using N_2 -adsorption/desorption isotherms conducted at 77 K, including surface area (S_{BET}), total pore volume (V_p), and mean pore radius (\bar{r}). These isotherms illustrated in Figure 7 belong to type-II with type H3 hysteresis loop according to universally-recognized authority on chemical nomenclature and terminology (IUPAC) classifications [31]. In particular, S_{BET} , V_p , and \bar{r} values are reported in Table 3. Interestingly, the nature of these isotherms reveals that the as-prepared solids are mesoporous as a function of capillary condensation starting at $P/P_0 = 0.5$.

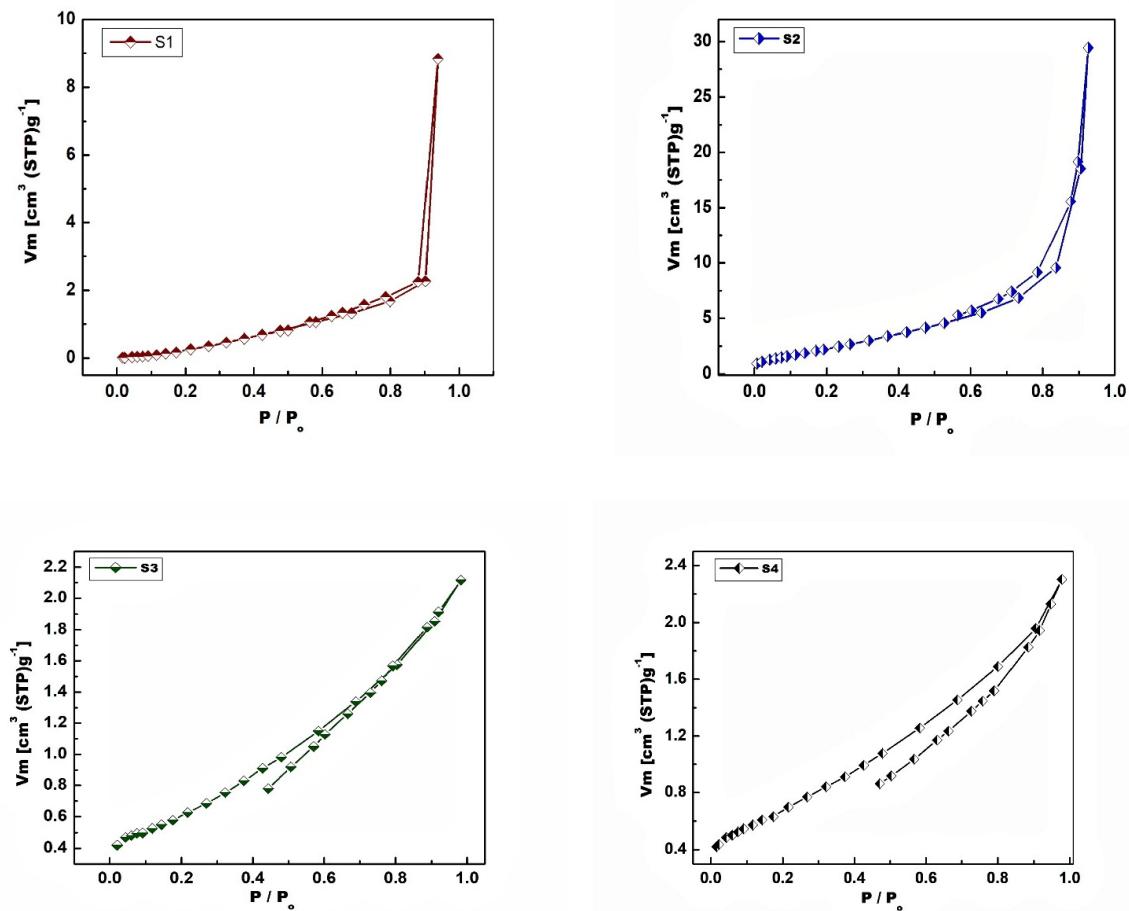


Figure 7. N₂-adsorption/desorption isotherms of the S1, S2, S3 and S4 samples.

Table 3. Surface properties for the S1, S2, S3 and S4 samples.

Samples	S_{BET} (m ² /g)	V_m (cc/g)	V_p (cc/g)	\bar{r} (nm)
S1	1.9923	0.4418	0.01367	28.430
S2	10.392	2.388	0.04552	17.430
S3	2.2995	0.5283	0.00327	5.6938
S4	2.5369	0.5829	0.0036	5.6149

The shape of isotherm with a jump in the adsorption process at high relative pressure ($P/P_0 = 0.90\text{--}0.93$) indicates the condensation process in inter particle voids. These voids were observed in TEM images of the S1 and S2 samples. This jump in the adsorption process cannot be observed in the isotherm of the S3 and S4 samples. One cannot ignore that our samples contain micropores depending upon such a jump in the adsorption process at low relative pressure ($P/P_0 = 0.05$) with subsequent low slope region. The S1 and S2 samples also have larger hysteresis loop area and range than the S3 and S4 samples, showing multilayer desorption from solid pore walls. Furthermore, the H3 hysteresis loop's form reveals slit-like pores or plate-like particles. This observation is supported by SEM and TEM investigations, which show that sheet-like structures are formed. The values of S_{BET} and V_p of the S2 sample are higher than those of the S1, S3, and S4 samples, according to the results shown in Table 3. Characterization of pore size distribution for the S1, S2, S3, and S4 samples depends upon non-local density functional theory (NLDFT) for

the adsorption of nitrogen in pores. The porosity or pore size distribution histograms of these samples are shown in Figure 8.

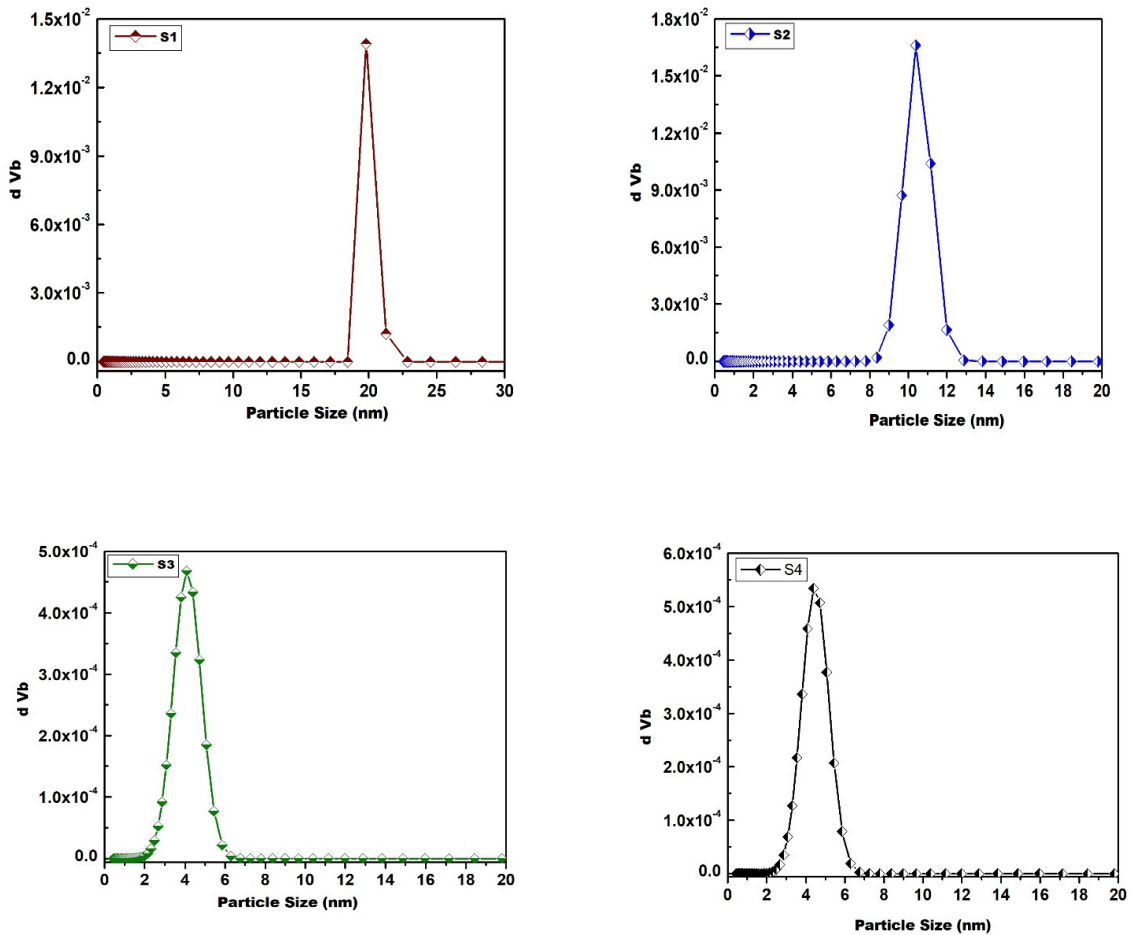


Figure 8. Pore size distribution for the of the S1, S2, S3 and S4 samples.

According to the observed pores with one model distribution, the majority of pores in the S1, S2, S3, and S4 solids are mesoporous at 19.802, 10.383, 4.0864, and 4.3903 nm, respectively.

3.5. Magnetic Properties

The magnetization (M) of copper-based composites measured at room temperature in ± 20 kOe applied magnetic field (H) is shown in Figure 9. Different types of magnetization curves are shown in this diagram, demonstrating varying magnetic properties of the as synthesized materials. The curves of the S1, S2, and S3 samples have an S-like form, showing that they are ferromagnetic at ambient temperature. These samples' room temperature ferromagnetism (RTFM) is caused by the same type of flaws, which are based on the same form and behavior of their magnetization curves. In addition, the curves of the S4 sample shows that this sample contains non-magnetic material (metallic copper) and another magnetic material (Cu_2O). Indeed, the XRD result of the S4 sample confirms that this sample consisted entirely of Cu and Cu_2O . The magnetic properties of these composites are presented in Table 4. However, the values of magnetization and coercivity enabled us to calculate the anisotropy constant ($K_a = H_c M_s / 0.98$) for different samples [32]. The relation between the anisotropy constant and the egg white content is illustrated in Figure 10. This figure displays that the S2 and S4 samples have low anisotropy. The opposite observation was depicted in the case of the S3 and S4 samples. In other words, increasing the egg white content up to 15 mL resulted in a decrease in the anisotropy inside the as-prepared specimen.

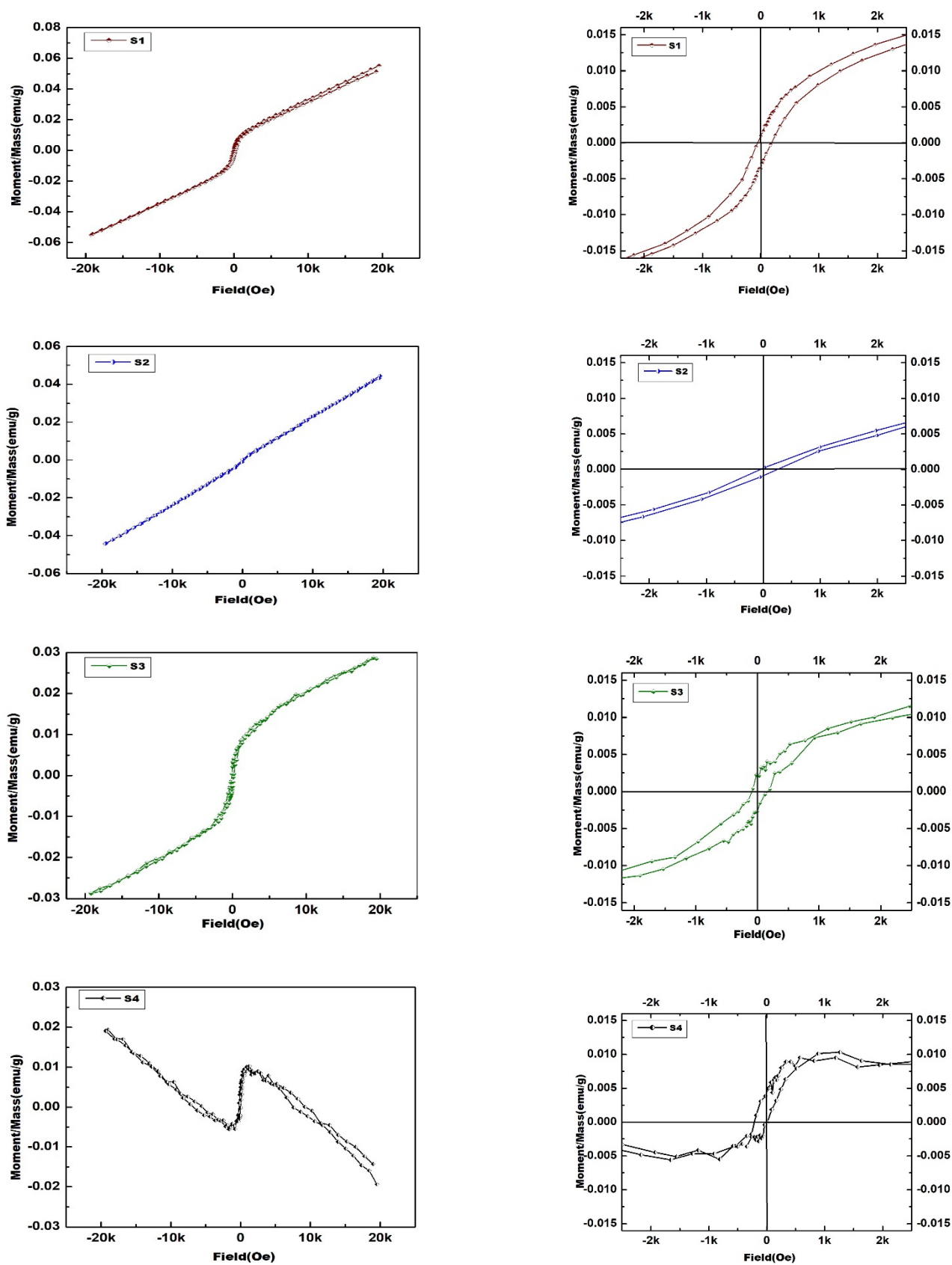
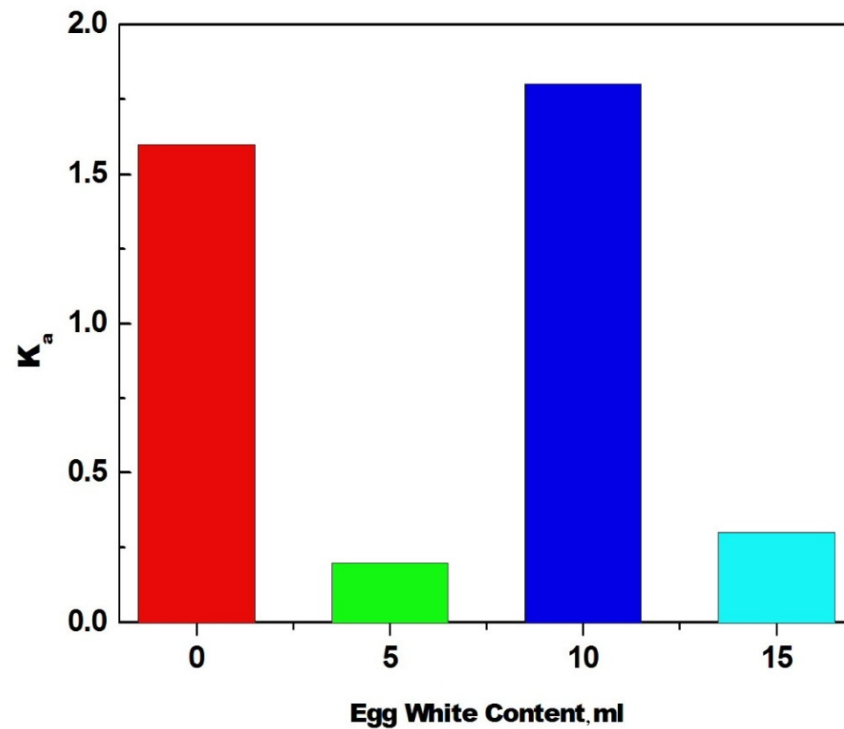


Figure 9. M-H curves of different nanocomposites measured at room temperature for S1, S2, S3 and S4 samples.

Table 4. The magnetic properties of the S1, S2, S3 and S4 samples.

Samples	M_s (emu/g)	M_r (emu/g)	M_r/M_s (emu/g)	H_c (Oe)
S1	0.0092	0.000094	0.10117	171
S2	0.0031	0.00045	0.1452	24
S3	0.0085	0.0021	0.2471	220
S4	0.0095	0.0049	0.5158	38

**Figure 10.** The relation between the anisotropy (K_a) of different nanocomposites with the egg white content of the S1, S2, S3 and S4 samples (red, green, blue, cyan, respectively).

4. Discussion

The main aim in this study was concentrated on the synthesis of different copper-based composites by using one pot. This process was achieved by using an attractive template such as the egg white mediated bio template. Considering egg white is a natural and biological fluid, it is amongst the most modern synthetic technologies based on green chemistry principles. However, it contains high concentrations of both amino acids and proteins, such as albumen and lysozyme [33]. These constituents can act as reducing, capping, and stabilizing agents in the preparation of nanomaterials [34]. In addition, egg white plays a controlling role in the shape of the prepared nano system [35]. Depending on our experience in this field and the information accessible in the literature, the egg white assumes multiple responsibilities in the preparation of copper-based composites in this study. It was used as fuel agent that stimulated the combustion process at 300 °C for a short time to obtain the final product. It plays a controlling role in the reduction of copper ions according to the amount used. However, it behaves as stabilizing agent by inhibiting the oxidation of the final product with oxygen from the surrounding environment. Consequently, the egg white mediated auto-combustion method resulted in the formation of different porous composites containing copper with multiple valences. XRD analysis confirms the previous roles observed in the S1, S2, S3, and S4 samples. Using a small (5 mL) or moderate (10 mL) amounts of egg white resulted in the fabrication of a composite containing Cu^{2+}/Cu^{1+} ions. On other hand, the 15 mL egg white-treated specimen was

composed of $\text{Cu}^{1+}/\text{Cu}^0$ ions due to the strong effects of the liberated reducing gases and presence of carbon traces. As a result of the egg white-assisted combustion technique used for this research, $\text{Cu}_2\text{O}/\text{CuO}$ and $\text{Cu}_2\text{O}/\text{Cu}$ nanocomposites were synthesized.

The attempt in this study was based on the identification of IR bands that are key to identifying these oxides, especially when they are present together inside composite. Based on both the literature and this study, we can confirm that CuO has IR bands in the range between 400 and 605 cm^{-1} . In addition, IR bands at $605\text{--}780\text{ cm}^{-1}$ and $876\text{--}825\text{ cm}^{-1}$ can be ascribed to Cu_2O particles. As the amount of egg white in the mixture increases, the position, intensity, and occurrence of most bands change. For example, increasing the egg white concentration contributed to the disappearance of several CuO bands, such as the bands at $876\text{--}825\text{ cm}^{-1}$, indicating a reduction in the amount of this oxide present and a subsequent cessation of it in the case of egg white-rich samples, as demonstrated in the S4 sample.

The presence of IR bands associated with hydroxyl groups indicates the presence of nanoparticles in the as synthesized systems. Furthermore, the bands associated to $\text{C}\text{--}\text{O}\text{--}\text{H}$ and $\text{C}\text{--}\text{H}$ confirms the presence of a carbon trace that was not visible using the XRD approach. In the synthesis of $\text{Cu}_2\text{O}/\text{CuO}$ and $\text{Cu}_2\text{O}/\text{Cu}$ nanocomposites, carbon traces and freed gases from the combustion process act as reducing and capping agents. Indeed, increasing the concentration of egg white increased the carbon content, resulting in an improvement in the copper reduction process from Cu^{2+} to Cu^{1+} to Cu . These observations were confirmed by XRD analysis.

Alterations in the physical properties and surface morphology of substances may require a change in the solids' surface characteristics. The phase transition, particle contraction or expansion, sintering, and crystallinity of materials could all be involved in the change in surface properties associated with structural changes [36]. Any change in the surface morphology of a material, on the other hand, resulted in a change in the surface characteristics due to the material's porosity and shape. As a result of the decrease in total pore volume and increase in mean pore radius, the surface area of the S1 sample is less than that of the S2 sample. These observations are supported by the decrease in the monolayer capacity (V_m) from 2.388 cc/g for the S2 sample to 0.4418 cc/g for the S1 sample. The decrease in SBET values for the S3 and S4 samples might be attributed to a drop in both V_p and V_m , as well as a phase transformation that resulted in extra Cu_2O or Cu particles. In fact, SEM and TEM analyses revealed that the porosity of the S2 sample is stronger than that of the S3 and S4 samples, indicating that surface morphology has an effect. It is expected that increasing the amount of egg white will increase the amount of released gases, leading to an increment in the number of pores, and consequently an increase in the surface area. However, the opposite behavior was observed due to the closure of most of these pores by some carbon, indicating the presence of pore blocking phenomena that resulted in a decrease in the SBET value.

In fact, the bulk of both cupric oxide and copper monoxide (CuO) and cuprous oxide (Cu_2O) demonstrate a antiferromagnetic (AFM) nature. The nanoparticles based on these oxides, in contrast, exhibit AFM associated with ferromagnetism (FM), resulting in unique magnetic characteristics. The intrinsic defects associated to complicated surface effects, including cation/anion vacancies, particle size effects, and uncompensated charges, could be the source of FM character in these oxides [37–39]. Cu valences at the CuO surface were indeed a mixture of $+1$ and $+2$ valence states [40]. The ferromagnetism of both CuO and Cu_2O nanoparticles was owing to a close association with the valence charged oxygen vacancies ($\text{Cu}^{1+}\text{--V}_\text{O}$) in both oxides, according to literature [41].

4.1. $\text{Cu}_2\text{O}/\text{CuO}$ Nanocomposites

XRD analysis showed that the S1, S2, and S3 samples consisted of Cu_2O and CuO phases with different phase ratios. Based on this analysis, these samples show contributions from ferromagnetic and paramagnetic components. So, one of aims this study is the determination of the room temperature ferromagnetism at the interface between CuO and

Cu₂O nanostructures. M-H curves for the S1, S2, and S3 samples depicted a clear S-like shape, indicating a typical signature of nominal FM-like solids. The ferromagnetism of the CuO/Cu₂O nanocomposites depends upon the different exchange interactions at the surface of these composites [42–44]. Indeed, the interface of CuO/Cu₂O nanocomposites consisted of three components containing Cu¹⁺ ions, Cu²⁺ ions, and V_o as oxygen vacancy. However, each oxygen vacancy provides one localized orbital with a large size and two doped electrons.

The different types of exchange interactions leading to the interface-related room temperature ferromagnetism of the CuO/Cu₂O nanocomposites can be classified as follows [45,46]: (i) Direct double exchange interaction (Cu¹⁺–V_o–Cu²⁺) containing a hop of the doped electrons between two different Cu ions via the V_o orbital, which resulted in a ferromagnetic alignment. (ii) Super exchange or an indirect double exchange interaction (Cu²⁺–V_o–Cu²⁺) containing a hop of the doped electrons between two Cu²⁺ ions via the V_o orbital to form the aligned ferromagnetic polaron. (iii) An additional ferromagnetic alignment (itinerant ferromagnetism) originates from the hop of spin-polarized electrons in each polaron between the different polarons. These interactions depend upon the phase or constituent ratios in CuO/Cu₂O nanocomposites [45].

In relation to the values of retentive, squareness, and coercivity, increasing the egg white concentration up to 15 mL resulted in a drop in the value of M_s for the as manufactured copper composite, and vice versa. The retentivity, squareness, and coercivity of different CuO/Cu₂O nanocomposites were associated with high anisotropy. However, the dislocation, strain, and stress in the constituents (CuO and Cu₂O) of these composites decrease by increasing of the egg white content. The values of the crystallite and/or particle sizes of these constituents showed the opposite behavior. As the sizes of the CuO/Cu₂O nanocomposites grew larger, the surface area of the CuO/Cu₂O nanocomposites reduced, as shown in the S3 sample. With these observations, it was expected that the magnetism would decrease by raising the egg white content to 15 mL. However, as seen in the S3 sample, the magnetism decreases as the temperature rises. The decrease in the concentration of oxygen vacancies at the surface or interface of the particles could be linked to the unexpected drop in the magnetization of CuO/Cu₂O nanocomposites. Finally, it can be concluded that the final ferromagnetism of CuO/Cu₂O nanocomposites is primarily determined by the oxygen vacancy content.

4.2. Cu₂O/Cu Nanocomposite

XRD measurements confirmed that the S4 sample was composed of Cu₂O/Cu nanocomposite. The M-H curve for the S4 samples showed contributions from ferromagnetic and diamagnetic components depending upon this sample consisting of a metallic copper (Cu) as a major phase and Cu₂O as a minor phase. The dislocation, strain, and stress in the constituents (Cu and Cu₂O) of these composites were observed with high values compared to those of the Cu₂O/CuO nanocomposites. The anisotropy of Cu₂O/Cu nanocomposite presents a low value, indicating a decrease in magnetostatic energy. The low value of anisotropy of Cu₂O/Cu nanocomposite is consistent with low coercivity of this composite. However, the polycrystalline mixtures of Cu₂O and Cu phases in the Cu₂O/Cu system resulted in the formation of multiple interfaces. These interfaces could be the cause of the magnetic and electric anomalies in the investigated composite [47]. The small magnetization of Cu₂O/Cu nanocomposite could be attributed to the super exchange interaction at the Cu₂O/Cu interface which creates a near-contact ferromagnetic layer depending upon the absence of magnetization for the metallic copper. In this exchange interaction, the V_o with two doped electrons can bound to Cu²⁺ ions, resulting in the aligned paramagnetic polaron.

5. Conclusions

Some significant data obtained in this allow for the following conclusions with regard to the major objectives:

1. The egg white assisted auto-combustion route is a simple, cheap, and quick method to prepare $\text{Cu}_2\text{O}/\text{Cu}$ and $\text{Cu}_2\text{O}/\text{CuO}$ nanocomposites. Furthermore, for the synthesis of $\text{Cu}_2\text{O}/\text{CuO}$ nanoparticles without the use of any additives, this method has several advantages, including economic feasibility, ease of scale-up, shorter processing time, and environmental friendliness. The crystallite size of the final products was clearly affected when the egg content employed in the preparation procedure was changed. Different elements (CuO , Cu_2O , and Cu) have crystallite sizes ranging from 32 to 51 nm, leading to nano phases. The dislocation, stress, and strain of various aspects of the final products were minimized when the amount of egg white was increased to 10 mL. In the case of the 15 mL egg white sample, the opposite behavior was observed.
2. The characteristics IR bands of both CuO and Cu_2O were observed with different intensities in the FTIR spectra of the S1, S2, and S3 samples. This indicates that these samples consisted of $\text{Cu}_2\text{O}/\text{CuO}$ composites. IR bands related CuO are not observed in the case of the S4 sample. The presence of carbon traces is confirmed by FTIR analysis, which is linked to an increase in the reduction process, which eventually leads to the formation of metallic copper, as shown in the S4 sample.
3. The egg white assisted combustion method brought about copper-based materials containing nano particles with different shapes. The as-prepared particles have an average grain size of 38 nm. Due to the small amount of egg white used, semi-spherical particles with a sheet-like structure formed. The high egg white concentration resulted in the development of several spherical particles on surface of the condensed sheet.
4. The surface properties of the produced solids were sensitive to structural and surface morphological changes. The surface area of the sample made with 5 mL of egg white is higher than that of the samples made with 0, 10, and 15 mL of egg white. The S1, S3, and S4 samples had smaller surface areas because the total pore volume of these samples was lower than the S2 sample. Furthermore, any contaminants will have an impact on the surface attributes. Indeed, due to pore bulking processes, the presence of an excess amount of carbon resulted in a decrease in the surface area of the as formed solids, particularly with the S4 sample.
5. The magnetization of $\text{Cu}_2\text{O}/\text{CuO}$ and $\text{Cu}_2\text{O}/\text{Cu}$ nanocomposites is affected by the concentration of egg white. The $\text{Cu}_2\text{O}/\text{Cu}$ nanocomposites demonstrated higher coercivity, dislocation, stress, and strain than the $\text{Cu}_2\text{O}/\text{CuO}$ nanocomposites. When the concentration of egg white was increased throughout the preparation process, the particle size of $\text{Cu}_2\text{O}/\text{CuO}$ nanocomposites increased, and the magnetization decreased as the oxygen vacancies at the surface/or interface of the particles decreased. The presence of nonmagnetic material (metallic copper) in $\text{Cu}_2\text{O}/\text{Cu}$ nanocomposites could be attributed to a decrease in oxygen vacancies.
6. The prepared composites are very important due to their various applications, such as catalytic materials, gas sensors, and magnetic storage media.
7. This environmentally friendly approach of producing $\text{Cu}_2\text{O}/\text{Cu}$ and $\text{Cu}_2\text{O}/\text{CuO}$ nanoparticles could be applied to the production of other industrially important metal oxides in the future.

Author Contributions: N.M.D., G.M.A.-S., S.I.A.-S., as well as O.H.A.-E.; technique, N.M.D., G.M.A.-S., S.I.A.-S., and O.H.A.-E.; program, O.H.A.-E.; validation, N.M.D., G.M.A.-S., S.I.A.-S., and O.H.A.-E.; formal analysis, N.M.D., G.M.A.-S., and O.H.A.-E.; systematic evaluation, N.M.D., G.M.A.-S., and O.H.A.-E.; inquiry, N.M.D. and G.M.A.-S.; resources, N.M.D., G.M.A.-S., and O.H.A.-E.; curation of results, N.M.D., G.M.A.-S., and O.H.A.-E.; writing—original preparation of the draft, N.M.D. and O.H.A.-E.; writing—review and editing, N.M.D., G.M.A.-S., and O.H.A.-E.; visualization, N.M.D. and O.H.A.-E.; supervision, N.M.D. and O.H.A.-E.; project management, N.M.D., G.M.A.-S., and O.H.A.-E.; procurement of financing, G.M.A.-S. and S.I.A.-S. All authors have read and agreed to the published version of the manuscript.

Funding: This research was funded by the Deanship of Scientific Research at Princess Nourah bint Abdulrahman University through the fast-track research-funding program.

Institutional Review Board Statement: Not applicable.

Informed Consent Statement: Not applicable.

Data Availability Statement: The data presented in this study are available on request from the corresponding author.

Acknowledgments: The authors would like to extend their sincere appreciation to Deanship of Scientific Research at Princess Nourah bint Abdulrahman University through the fast-track research-funding program.

Conflicts of Interest: The authors declare no conflict of interest.

References

1. Sankar, R.; Manikandan, P.; Malarvizhi, V.; Fathima, T.; Shivashangari, K.S.; Ravikumar, V. Green synthesis of colloidal copper oxide nanoparticles using *Carica papaya* and its application in photocatalytic dye degradation. *Spectrochim. Acta Part A Mol. Biomol. Spectrosc.* **2014**, *121*, 746–750. [[CrossRef](#)]
2. George, M.; Britto, S.J. Biosynthesis, characterization, antimicrobial, antifungal and antioxidant activity of copper oxide nanoparticles (CONPS). *Eur. J. Biomed. Pharma. Sci.* **2014**, *1*, 199–210.
3. Dhineshbabu, N.R.; Rajendran, V.; Nithyavathy, N.; Vetumperumal, R. Study of structural and optical properties of cupric oxide nanoparticles. *Appl. Nanosci.* **2016**, *6*, 933–939. [[CrossRef](#)]
4. Iravani, S. Green synthesis of metal nanoparticles using plants. *Green Chem.* **2011**, *13*, 2638–2650. [[CrossRef](#)]
5. Ren, G.; Hu, D.; Cheng, E.W.; Vargas-Reus, M.A.; Reip, P.; Allaker, R.P. Characterisation of copper oxide nanoparticles for antimicrobial applications. *Int. J. Antimicrob. Agents* **2009**, *33*, 587–590. [[CrossRef](#)]
6. Yallappa, S.; Manjanna, J.; Sindhe, M.A.; Satyanarayan, N.D.; Pramod, S.N.; Nagaraja, K. Microwave assisted rapid synthesis and biological evaluation of stable copper nanoparticles using *T. arjuna* bark extract. *Spectrochim. Acta Part A Mol. Biomol. Spectrosc.* **2013**, *110*, 108–115. [[CrossRef](#)] [[PubMed](#)]
7. Kwak, K.; Chongyoun, K. Viscosity and thermal conductivity of copper oxide nanofluid dispersed in ethylene glycol. *Korea-Aust. Rheol. J.* **2005**, *17*, 35–40.
8. Stoimenov, P.K.; Rosalyn, L.; Klinger, L.; George, L.M.; Kenneth, J.K. Metal oxide nanoparticles as bactericidal agents. *Langmuir* **2002**, *18*, 6679–6686. [[CrossRef](#)]
9. Diaz-Droguett, D.E.; Espinoza, R.; Fuenzalida, V.M. Copper nanoparticles grown under hydrogen: Study of the surface oxide. *Appl. Surf. Sci.* **2011**, *257*, 4597–4602. [[CrossRef](#)]
10. Mortimer, M.; Kasemets, K.; Kahru, A. Toxicity of ZnO and CuO nanoparticles to ciliated protozoa *Tetrahymena thermophile*. *Toxicology* **2010**, *269*, 182–189. [[CrossRef](#)]
11. Devaraj, M.; Saravanan, R.; Deivasigamani, R.; Vinod Kumar Gupta, V.K.; Gracia, F.; Jayadevan, S. Fabrication of novel shape Cu and Cu/Cu₂O nanoparticles modified electrode for the determination of dopamine and paracetamol. *J. Mol. Liq.* **2016**, *221*, 930–941. [[CrossRef](#)]
12. Zhang, Q.; Zhang, K.; Xu, D.; Yang, G.; Huang, H.; Nie, F.; Liu, C.; Yang, S. CuO nanostructures: Synthesis, characterization, growth mechanisms, fundamental properties, and applications. *Prog. Mater. Sci.* **2014**, *60*, 208–337. [[CrossRef](#)]
13. Devi, A.B.; Moirangthem, D.S.; Talukdar, N.C.; Devi, M.D.; Singh, N.R.; Luwang, M.N. Novel synthesis and characterization of CuO nanomaterials: Biological applications. *Chin. Chem. Lett.* **2014**, *25*, 1615–1619. [[CrossRef](#)]
14. Parveen, F.; Sannakki, B.; Mandke, M.V.; Pathan, H.M. Copper nanoparticles: Synthesis methods and its light harvesting performance. *Sol. Energy Mater. Sol. Cells.* **2016**, *144*, 371–382. [[CrossRef](#)]
15. Lashanizadegan, M.; Erfaninia, K. Synthesis, characterization and catalytic property of CuO and Ag/CuO nanoparticles for the epoxidation of styrene. *Korean J. Chem. Eng.* **2013**, *30*, 2007–2011. [[CrossRef](#)]
16. Suleiman, M.; Mousa, M.; Hussein, A.; Hammouti, B.; Hadda, T.B.; Warad, I. Copper (II)-oxide nanostructures: Synthesis, characterizations and their applications—review. *J. Mater. Environ. Sci.* **2013**, *4*, 792–797.
17. Karunakaran, C.; Manikandan, G.; Gomathisankar, P. Microwave, sonochemical and combustion synthesized CuO nanostructures and their electrical and bactericidal properties. *J. Alloys Compd.* **2013**, *580*, 570–577. [[CrossRef](#)]
18. Kumar, P.P.N.V.; Shameem, U.; Kollu, P.; Kalyani, R.L.; Pammi, V.N. Green synthesis of copper oxide nanoparticles using aloe vera leaf extract and its antibacterial activity against fish bacterial pathogens. *BioNanoScience* **2015**, *5*, 135–139. [[CrossRef](#)]
19. Han, Z.D.; Wu, Z.; Wang, S.; Yang, S. Oriented Mn-doped CuO nanowire arrays. *Nanotechnology* **2016**, *27*, 135603–135610. [[CrossRef](#)]
20. Yang, Y.; Xu, D.; Wu, Q.; Diao, P. Cu₂O/CuO bilayered composite as a high-efficiency photocathode for photo electrochemical hydrogen evolution reaction. *Sci. Rep.* **2016**, *6*, 35158. [[CrossRef](#)]
21. Han, J.; Zong, X.; Zhou, X.; Li, C. Cu₂O/CuO photocathode with improved stability for photoelectrochemical water reduction. *RSC Adv.* **2015**, *5*, 10790–10794. [[CrossRef](#)]
22. Cullity, B.D. *Elements of X-ray Diffraction*; Addison-Wesley Publishing Co. Inc.: Singapore, 1976; Chapter 14.
23. Shaltout, A.A.; Abd-Elkader, O.H. The role of gas direction in a modified Grimm-type glow discharge for controlling the degree of crystallinity in brass alloy thin films. *Vacuum* **2015**, *121*, 105–112. [[CrossRef](#)]

24. Abd-Elkader, O.H.; Deraz, N.M. Synthesis and characterization of new copper based nanocomposite. *Int. J. Electrochem. Sci.* **2013**, *8*, 8614–8622.
25. Boultif, A.; Louer, D. Powder pattern indexing with the dichotomy method. *J. Appl. Cryst.* **2004**, *37*, 724–731. [[CrossRef](#)]
26. Dubal, D.; Dhawale, D.S.; Salunkhe, R.; Jamdade, V.; Lokhande, C.D. Fabrication of copper oxide multilayer nanosheets for supercapacitor application. *J. Alloys Compd.* **2010**, *492*, 26–30. [[CrossRef](#)]
27. Ethiraj, A.S.; Kang, D.J. Synthesis and characterization of CuO nanowires by a simple wet chemical method. *Nanoscale Res. Lett.* **2012**, *7*, 70–75. [[CrossRef](#)]
28. Alhumaimess, M.S.; Essawy, A.A.; Kamel, M.M.; Alsohaimi, I.H.; Hassan, H.M.A. Biogenic-mediated synthesis of mesoporous Cu₂O/CuO nano-architectures of superior catalytic reductive towards nitroaromatics. *Nanomaterials* **2020**, *10*, 781. [[CrossRef](#)]
29. Kumar, B.; Smita, K.; Debut, A.; Cumbal, L. Andean sacha inchi (*Plukenetia Volubilis* L.) leaf-mediated synthesis of Cu₂O Nanoparticles: a low-cost approach. *Bioengineering* **2020**, *7*, 54. [[CrossRef](#)]
30. Nie, L.; Yu, J.; Li, X.; Cheng, B.; Liu, G.; Jaroniec, M. Enhanced performance of Na OH-modified Pt/TiO₂ toward room temperature selective oxidation of formaldehyde. *Environ. Sci. Technol.* **2013**, *47*, 2777–2783. [[CrossRef](#)]
31. Sing, K.S.W. Reporting physisorption data for gas/solid systems with special reference to the determination of surface area and porosity (Provisional). *Pure Appl. Chem.* **1982**, *54*, 2201–2218. [[CrossRef](#)]
32. Pitike, K.C.; Marquez-Rossy, A.E.; Flores-Betancourt, A.; Chen, D.; Santosh, K.; Cooper, V.R.; Lara-Curzio, E. On the elastic anisotropy of the entropy-stabilized oxide (Mg, Co, Ni, Cu, Zn)O compound. *J. Appl. Phys.* **2020**, *128*. [[CrossRef](#)]
33. Lai, B.H.; Yeh, C.C.; Chen, D.H. Surface modification of iron oxide nanoparticles with polyarginine as a highly positively charged magnetic nano-adsorbent for fast and effective recovery of acid proteins. *Process Biochem.* **2012**, *47*, 99–105. [[CrossRef](#)]
34. Al-Senani, G.M.; Deraz, N.M.; Abd-Elkader, O.H. Magnetic and characterization studies of Co/Co₃O₄ nanocomposite. *Processes* **2020**, *8*, 844. [[CrossRef](#)]
35. Al-Senani, G.M.; Abd-Elkader, O.H.; Al-Kadhi, N.S.; Deraz, N.M. Effect of the glycine treatment on synthesis and physicochemical characterization of nanosized Ni-Mn mixed oxides. *Crystals* **2021**, *11*, 487. [[CrossRef](#)]
36. Deraz, N.M.; Shaban, S. Optimization of catalytic, surface and magnetic properties of nanocrystalline manganese ferrite. *J. Anal. Appl. Pyrolysis* **2009**, *86*, 173–179. [[CrossRef](#)]
37. Arbuzova, T.I.; Smolyak, I.B.; Naumov, S.V.; Samokhvalov, A.A. Effect of doping on the magnetic properties of the low-dimensional antiferromagnet CuO. *Phys. Solid State* **1998**, *40*, 1702–1705. [[CrossRef](#)]
38. Muraleedharan, K.; Subramaniam, C.K.; Venkataramani, N.; Rao, G.T.K.; Srivastava, C.M.; Sankaranarayan, V.; Srinivasan, R. On the magnetic susceptibility of CuOx. *Solid State Commun.* **1990**, *76*, 727–730. [[CrossRef](#)]
39. Punnoose, A.; Magnone, H.; Seehra, M.S.; Bonevich, J. Bulk to nanoscale magnetism and exchange bias in CuO nanoparticles. *Phys. Rev. B Condens. Matter* **2001**, *64*, 1–8. [[CrossRef](#)]
40. Gao, D.; Zhang, J.; Zhu, J.; Qi, J.; Zhang, Z.; Sui, W.; Shi, H.; Xue, D. Vacancy-mediated magnetism in pure copper oxide nanoparticles. *Nanoscale Res. Lett.* **2010**, *5*, 769–772. [[CrossRef](#)]
41. Gao, D.; Yang, Z.; Zhang, J.; Yang, G.; Zhu, Z.; Qi, J.; Si, M.; Xue, D. Transforming from paramagnetism to room temperature ferromagnetism in CuO by ball milling. *AIP Adv.* **2011**, *1*. [[CrossRef](#)]
42. White, J.S.; Bator, M.; Hu, Y.; Luetkens, H.; Stahn, J.; Capelli, S.; Das, S.; Döbeli, M.; Lippert, T.; Malik, V.K.; et al. Strain-induced ferromagnetism in antiferromagnetic LuMnO₃ thin films. *Phys. Rev. Lett.* **2013**, *111*. [[CrossRef](#)]
43. Sun, H.Y.; Zhang, H.M.; Hou, X.; Liu, L.H.; Wu, T.S.; Yang, S.M. Significant room temperature ferromagnetism in PAA thin films. *J. Mater. Chem. C* **2013**, *1*, 3569–3572. [[CrossRef](#)]
44. Hu, L.; Huang, J.; He, H.; Zhu, L.; Liu, S.; Jin, Y.; Sun, L.; Ye, Z. Dual-donor (Zn and VO) mediated ferromagnetism in copper-doped ZnO micron-scale polycrystalline films: A thermally driven defect modulation process. *Nanoscale* **2013**, *5*, 3918–3930. [[CrossRef](#)]
45. Gao, D.; Zhang, Z.; Xu, Q.; Zhang, J.; Yan, Z.; Yao, J.; Xue, D. Room temperature ferromagnetism in CuO/Cu₂O microspheres: Towards interface effect. *Appl. Phys. Lett.* **2014**, *104*. [[CrossRef](#)]
46. Heng, T.S.; Qi, D.C.; Berlijn, T.; Yi, J.B.; Yang, K.S.; Dai, Y.; Feng, Y.P.; Santoso, I.; Sánchez-Hanke, C.; Gao, X.Y.; et al. Room-temperature ferromagnetism of Cu-Doped ZnO Films probed by soft X-ray magnetic circular dichroism. *Phys. Rev. Lett.* **2010**, *105*. [[CrossRef](#)]
47. Samokhvalov, A.A.; Arbusova, T.I.; Viglin, N.A.; Naumov, S.V.; Galakhov, V.R.; Zatsopin, D.A.; Kotov, Y.A.; Samatov, O.M.; Kleshchev, D.G. Paramagnetism in copper monoxide systems. *Phys. Solid State.* **1998**, *40*, 268–271. [[CrossRef](#)]